LAWRENCE
LIVERMORE
NATIONAL
LABORATORY

LLNL-JRNL-416030

Long-term Observations of the Convective Boundary Layer Using Insect Radar Returns at the SGP ARM Climate Research Facility

Arunchandra S. Chandra, Pavlos Kollias, Scott E. Giangrande, Stephen A. Klein

August 24, 2009

Journal of Climate

Disclaimer

Long-term Observations of the Convective Boundary Layer Using Insect Radar Returns at the SGP ARM Climate Research Facility

Arunchandra S Chandra, Pavlos Kollias and Scott E. Giangrande

Department of Atmospheric and Oceanic Sciences

McGill University, Montreal, Quebec Canada

Stephen A. Klein

Atmospheric, Earth, and Energy Division

Lawrence Livermore National Laboratory, Livermore, California

Submitted to: *Journal of Climate*

Author`s email: arunchandra.chandra@mail.mcgill.ca

McGill University

Department of Atmospheric and Oceanic Sciences

805 Sherbrooke Street West

Montreal, Quebec, H3A 2K6, Canada

Abstract

A long-term study of the turbulent structure of the convective boundary layer (CBL) at the US Department of Energy Atmospheric Radiation Measurement (ARM) program Southern Great Plains (SGP) Climate Research Facility is presented. Doppler velocity measurements from insects occupying the lowest 2 km of the boundary layer during summer months are used to map the vertical velocity component in the CBL. The observations cover four summer periods (2004-2008) and are classified into cloudy and clear boundary layer conditions. Profiles of vertical velocity skewness and variance are estimated to study the daytime evolution of the convective boundary layer during these conditions. A conditional sampling method is applied to the original Doppler velocity dataset to extract coherent vertical velocity structures and examine plume dimension and contribution to the turbulent transport. Overall, the derived turbulent statistics are consistent with previous aircraft observations and suggested analytical profiles. The observations provide unique insight into the daytime evolution of the convective boundary layer and the role of increased cloudiness in the turbulent budget of the subcloud layer. Coherent structures (plumes) are found responsible for more than 80% of the total turbulent transport resolved by the cloud radar system. The extended data set is suitable for evaluating boundary-layer parameterizations for a variety of surface and cloud conditions.

1. INTRODUCTION

The representation of clear and cloudy boundary layer conditions in Global Climate Models (GCMs) is relatively poor, thereby limiting the predictability of cloud feedback in a changing climate (Tiedtke 1989; Bony et al., 2006; Teixeira et al., 2008). Over land, shallow cumuli coverage is 5%, significant to affect the global radiation budget (e.g., Norris, 1998). This shallow mode of convection over land also plays an important role in the preconditioning of deep convection (Lenderink et al., 2004). A controlling factor in the transition and evolution of clear and cloud boundary layers is the diurnal cycle of the convective boundary layer (CBL), where turbulence is the main transport mechanism for the redistribution of momentum, energy and moisture. The turbulent structure of the CBL exhibits a strong diurnal cycle as a result of the interaction between the surface and the cloud layer above (e.g., Hogan et al., 2008; Moyer and Young, 1991). Turbulent flux in the boundary layer is often parameterized in terms of large eddies that are responsible for the bulk of the transport. Some of these large thermals (updrafts) are considered the invisible roots of the clouds in the subcloud layer. One key challenge is to understand what regulates the mass flux of subcloud air into the cloud layer, its diurnal cycle and the impact of clouds (Siebesma et al., 2003).

Previous observational CBL studies considered only cloud-free conditions (e.g., Lenschow 1970; Kaimal et al., 1976; Young, 1988). Coupled studies of the cloud and subcloud layer are limited to aircraft and tower measurements (e.g., Lemone and Pennell, 1976; Warner 1977), data obtained from tethered balloon systems (e.g., Echternacht and Garstang, 1976, Thompson et al., 1980) and multiple radiosonde ascents (e.g., Johnson, 1977). These previous efforts emphasize profiling the vertical structure of the CBL with coarse resolution and are limited in duration due to inhibiting costs associated with research aircrafts. Nevertheless, these

studies indicate that the standard similarity theory based on surface fluxes using tower measurements is not sufficient (eg., Kaimal and Finnigan 1994; Rao and Narasimha 2006) and clearly fails near the subcloud layer top in shallow cumulus conditions (e.g., Nicholls and Lemone 1980). An additional approach applied to study the interaction of the cloud and subcloud layer is budget studies (e.g., Betts 1976; Brummer 1978). These methods implicitly consider the average effects of the transport mechanisms at scales of at least 10^4 km^2 and time periods in excess of an hour (Nicholls and Lemone, 1980). As a consequence, this approach is insufficient to resolve the shallow cumulus clouds of diameters less than a few of km.

Over the last few decades, large-eddy simulation (LES) has become an important tool for boundary layer research. Due to typically high spatial and temporal resolutions, LES is suitable for studying conditionally sampled properties of shallow cumulus clouds (e.g., Schumann and Moeng 1991; Siebesma and Cuijpers 1995; Wang and Stevens 2000; De Roode and Bretherton 2003). Despite encouraging results, important LES findings for shallow cumulus clouds remain unsupported by observations (Neggers et al., 2003) mainly due to the scarcity of in-cloud observations and insufficient knowledge about turbulent structure of the subcloud layer. Turbulent statistics (velocity variance, skewness, mass-flux, etc.) from LES and single column models (SCM) have been successfully compared with observations for individual case study (e.g., Lenderink et al., 2004, Brown et al., 2002, Siebesma et al., 2003; Neggers et al., 2003; Stevens et al., 2001), but cover only a limited set of conditions. This deficiency hints at the need for long-term measurements on subcloud layer turbulence for a variety of conditions to derive the adequate statistics for model evaluation.

Progress in ground-based remote sensors for atmospheric boundary layer research offers an opportunity for accurate measurements of basic boundary layer parameters (profiles of

temperature, wind, moisture, surface fluxes, etc). A thorough review on the contributions and limitations of these surface-based instruments until the 1990s is discussed elsewhere (Wilczak et al, 1996). Cloud radars and Doppler lidar provide measurements in cloud and clear conditions with resolutions adequate for conditional sampling studies (Kollias et al, 1999; Kollias et al, 2000; Kollias et al 2001a; Kollias et al 2002; French et al, 2000; Hogan et al, 2008), but to date there are no long-term observational studies on the subcloud structure of shallow cumulus.

Echoes from non-hydrometeor targets including insects have been reported within many low altitude radar observations, both in clear and cloudy boundary layer (e.g., Achtemeier 1991; Russel and Wilson 1997; Clothiaux et al, 2000). Cloud radar observations have been previously used in entomology to study flights of small insects (weight ~ 2 mg) because of its sensitivity of these systems to detect small insects (Riley, 1992, Ka-band, 35 GHz). In a meteorological context, echoes from nonhydrometeor scatterers including insects should be removed from hydrometeor echoes from the MMCR for the study of clouds.

In the present study, a different approach is adopted for long-term CBL study. Instead of removing the insect MMCR echo contribution to study clouds in the boundary layer, this study capitalizes on insect Doppler content to study the turbulent structure of the subcloud layer. Here, insects are treated largely as passive scatterers that follow the mean vertical air motion (air tracers). Doppler signatures of insect echoes measured from cloud radar (95 GHz, 3 mm) were previously explored to study the characteristics of buoyant eddies within CBL using 3 days of data during International H_2o Project (IHOP-2002) (Miao, Geerts and Lemone 2006). For this study, a more extensive set of insect observations from Doppler radar are classified into clear and cloudy boundary layer (non precipitating shallow cumulus) conditions and diurnal composite profiles of vertical velocity variance, skewness and updraft mass flux are computed. In addition

to the long-term MMCR data set, supplementary observations from the Radar Wind Profiler (RWP), Total Sky Imager and tower observations are used to characterize the surface conditions and the top of the mixed layer.

2. OBSERVATIONS

The US Department of Energy Atmospheric Radiation Measurement (ARM) program Southern Great Plains (SGP) Climate Research Facility (ACRF) in Lamont, OK (36.605^{o} N, 97.485^{o} W, Altitude: 318 m MSL) provides continuous long-term sampling of the atmosphere from synergetic instruments (e.g., Stokes and Schwartz, 1994; Ackerman and Stokes, 2003; Kollias et. al 2007). This study capitalizes on several routinely generated ARM products including the Active Remote Sensing Cloud Location (ARSCL) product (Clothiaux et al., 2000), which combines information from the vertically pointing 35-GHz (Ka-band, 8.66 mm wavelength) Millimeter Cloud Radar (MMCR, e.g., Moran et al 1998; Kollias et al. 2007), a Belfort Laser Ceilometer and a Micropulse Lidar at a temporal resolution of 10 s and vertical (gate) resolution of 45 m.

The MMCR measurements are used to characterize the cloud (scattering from hydrometeors) and subcloud (scattering from insects) layer. Typically, removing insect echoes from hydrometeor populations is problematic because of the similar range of reflectivity of insects to those of the clouds (Clothiaux et al, 2000). Especially during summer months, MMCR (34.86 GHz, 8.66 mm) data from the ARM facility at SGP has dominant insect echoes (Luke et al, 2008). Weakly flying insects are observed in the "finelines" of the clear air radar echoes and high reflectivity regions are attributed to the high density of insects (Russell and Wilson, 1997). Figure 1a,b shows the diurnal variation of MMCR reflectivity and Doppler velocity during shallow cumulus conditions. In the figure, the cloud bases are associated with the high reflectivity region and updraft motion beneath. The echo plumes are expected to represent coherent eddies of rising motion and in most of the fair-weather CBL, these echoes are believed

to be small insects (< 10 mm in flights, e.g., Miao, Geerts and Lemone 2006). According to the hypothesis tested and verified in Geerts and Miao (2005; Here after GM05), these scatterers are subject to turbulent mixing in the CBL and tend to converge in the regions of sustained ascent as these insects oppose any updrafts in which they embedded.

A collocated 915-MHz Radar Wind Profiler (RWP), a Total Sky Imager (TSI) and a CO_2 flux system provide supplemental observations. The RWP collects profiles of wind speed/direction and radar reflectivity factor from hydrometeors and refractive index inhomogeneities at a 30 s temporal and 60 m vertical resolution up to 2.4 km AGL. The CO_2 flux system at the SGP central facility consists of a 60 m tower with three sets of instruments installed at 4.5 m (surface), 25 m and 60 m. Each instrument set contains a sonic anemometer at 10 Hz that measures orthogonal component of wind velocity (u, v and w) and a sonic temperature sensor (which approximates virtual temperature in K). Turbulent fluxes (e.g., sensible, latent) for this study are only computed from the sonic measurements obtained at the surface.

Observations were collected during the June-September (JJAS) period and for the years 2004 to 2007 at the SGP ACRF. The JJAS period was selected due to the presence of the deepest insect layer during that period and in part for the favourable conditions for undisturbed clear and cloud boundary layer conditions. Ambient cloud conditions are assigned according to the output from the collocated ceilometer and TSI. The ceilometer records the fraction of hourly coverage of clouds over the site and the TSI records a sky opaqueness fraction as well as a visual image record useful to remotely identify clear and cumulus event hours. Cloud fractions for shallow cumulus events have also been recorded into ceilometer-based groupings of low (>0 - 20%), medium (20 - 60%) and high (60 -100%) hourly fraction of clouds**.** Additional confirmation for

non-precipitating conditions is provided by available surface rain gauge measurements, cloud base precipitation flags and MMCR radar reflectivity thresholds.

3. METHODOLOGY

For every hour of observations, profiles of the vertical velocity variance and skewness, updraft fraction and mass flux are estimated. In addition, coherent vertical velocity structures are objectively identified and estimates of their dimensions and contribution to the total mass flux are provided. In detail, the data post-processing includes the following steps:

3.1 MMCR Insect Layer Top Detection and Removal of Downward Doppler Bias

The primary observations in this study are MMCR cloud radar insect echoes in the CBL (e.g., Riley 1992; Russel and Wilson 1997; Clothiaux et al, 2000; Luke et al., 2008). Again, insect-based MMCR echoes are regularly observed during the warm season (April-October). Using the ceilometer, rain gauge and TSI measurements, one can verify that these returns do not originate from hydrometeors. A limiting factor for the vertical extent of the insect echoes is temperature and clouds (Luke et al., 2008). Insects are assumed to capitalize on large thermals in the CBL to change their altitude (Fig. 1b) and in turn, the insect Doppler signatures are useful to track the spatial scales and magnitude of large eddies in the CBL. Nevertheless, since insects are not passive tracers of air motion, it is important to consider the contribution of insect vertical motion on the observed MMCR Doppler velocity.

Long-term velocity observations from the MMCR dataset in clear sky conditions indicate a net downward velocity of magnitude 0.2 - 0.4 m/s in the lower half of the CBL that approaches zero near the insect layer top. The insect layer top is defined as the maximum height where we observe MMCR echoes from biological/insect media more than 80% of the time within an hour.

The insect layer top is commonly observed slightly below the CBL top. A similar downward velocity observation has been reported following the airborne measurements of the Wyoming cloud radar during the IHOP-2002 field campaign over the SGP location (GM05). To mitigate the contribution of insect velocity from the MMCR mean Doppler velocity measurements as part of basic pre-processing, an hourly mean Doppler velocity of zero is assumed in the insect layer. Thus, the insect induced downward bias is removed at each height every hour and our estimate of the turbulent statistics is based on the velocity perturbation.

3.2. Conditional Sampling of Coherent Vertical Velocity Structures

Large Eddy Simulation (LES) models are developed upon the hypothesis that these models have sufficient resolution to resolve the length of eddies that are responsible for most of the turbulent transport in the boundary layer. One of the main motivations of the study is to examine to what extent the turbulent transport in the CBL is performed by large coherent eddies and to investigate the corresponding spatial dimensions of these plumes. Both tasks require the detection of coherent vertical velocity structures (plumes) using an objective conditional sampling (e.g., Kollias and Albrecht, 2000).

MMCR observations are provided in time and height. Time is converted to horizontal distance using the hourly consensus estimates of the horizontal wind magnitude from the RWP. The minimum horizontal dimension of a coherent velocity structure (plume) is the distance an air mass can travel in 30 sec due to the horizontal wind in the boundary layer. This translates to a minimum horizontal width of 150 to 300 m for typical horizontal winds of 5 to 10 ms^{-1} in the boundary layer.

For this study, the general requirements are that all points contributing to an updraft plume must have an upward Doppler velocity and the minimum vertical extent of the plumes is set to 225 m (5 MMCR range gates) and 30 sec (3 MMCR profiles). Thus, the effective time-height filter to conditionally sample plumes is a 3x5 boxcar filter applied to the Doppler velocity perturbation field (Fig 2b) using a velocity threshold (e.g., zero). Higher updraft velocity magnitudes (e.g., 0.3 – 1.0 ms^{-1}) are used to identify more intense plumes. Once the area (time-height) covered with plumes is detected, the plume contribution to the mass flux can be estimated for different velocity thresholds (here, a velocity threshold of 0 m/s is assumed). The observed widths are normalized by the cloud base and mixed layer height during shallow cumulus and clear-sky conditions, respectively (estimates of these heights described in Section 3.3). Best-fit exponential curves are fitted to the distributions of observed plume widths for updraft and downdraft structures and the half-width's (Distance at which the best-fit exponential curve attains 0.5 times the smallest resolvable scale) are recorded (e.g., as in Miao et al., 2006) as a measure of the median width in the observed distributions.

3.3. Estimation of Mixed-Layer Height (MLH)

The normalization of vertical profiles with height (as required above and in Section 4, Eq. 1) capitalizes on an estimate of the boundary layer depth at various points throughout daytime hours. During cumulus-topped conditions, the cloud base heights from the ceilometer are used to estimate the MLH. During clear sky conditions, no hydrometeor scatterers are present for the laser to detect and an alternative approach is needed. Although the MLH can be estimated from available ARM sounding data using the gradient of the virtual potential temperature, such estimates are not available at the resolution required for hourly scaling. A reasonable

approximation for MLH designation may also be accomplished using the 915-MHz RWP that is highly sensitive to Bragg scattering from gradients of the atmospheric refractive index. These gradients are very strong at the top of the mixed-player due to the presence of strong gradients in the temperature and humidity field. The RWP measurements also match a desired temporal resolution for accurate turbulence and skewness profile calculations. For this purpose, an automatic procedure was developed to trace the regions of the maximum reflectivity gradient in the RWP field as a proxy for the top of the mixed layer. An example of RWP-retrieved mixed layer heights (black circles) as compared with the two estimates obtained from collocated ARM radiosonde launches (red crosses) is located in Fig. 1c.

4. ANALYSIS

A total of 2,894 hours of observations over four years (2004 - 2007) of summer periods were included in this analysis (Tables 1-4). The events are separated into clear sky periods (1,603 hours) and cumulus-topped boundary layer periods (1,291 hours). The cumulus-topped cases are further classified with respect to cloud fraction as: low (cloud fraction less than 20% of the hour, 412 hours), moderate (cloud fraction between 20% and 60%, 516 hours) and high (cloud fraction above 60%, 363 hours).

i. Bulk Daytime Observations from the Dataset (Tables 1-4)

During cloud free conditions, the mixed-layer depth increases from 648 m at 08:00 LST to a maximum of 1654 m at 16:00 LST. In cumulus-topped conditions, the largest variability in the cloud base height is during low cloud fraction conditions (1080 to 1730 m) and the smallest during high cloud fraction conditions (1154 – 1401 m). In general, the cloud base height decreases with increasing cloud fraction. The surface buoyancy flux maximum is observed around local noon and decreases from 275 Wm^{-2} during clear skies conditions to 233, 217 and 154 for low, moderate and high cloud fraction conditions, respectively. This change in the surface buoyancy flux reflects the shortwave forcing of low-level liquid clouds.

The convective velocity scale in Tables 1-4 is defined as

$$w_* = \left(\frac{g}{T_v}\overline{w'T'_v}h\right)^{1/3}, \qquad (1)$$

where g is the acceleration due to gravity, T_v is the virtual temperature, $\overline{w'T'_v}$ is the surface kinematic buoyancy flux and h is the boundary layer depth. In (1), the kinematic buoyancy flux can be computed directly from available surface ARM sonic measurements of w' and T'_v. The calculated convective velocity scale maximum is also observed at local noon and its value is around 2.0 – 2.1 ms^{-1} for clear skies, low and moderate cloud conditions. Significant drop in the convective velocity scale maximum (1.65 ms^{-1}) is observed during high cloud fraction conditions.

In addition to the surface conditions, the daytime evolution of the mixed-layer and subcloud layer top heights are important for characterizing the vertical extend of the convective boundary layer (Fig. 2). During clear-skies conditions, the mixed-layer top height elevates from 1.2 km at 09:00 LST to 1.8 km at 16:00 LST. During cumulus-topped conditions, the subcloud layer top exhibits smaller variability (1.4 to 1.7 km). Fig. 2 shows the estimate of insect layer top for both clear-skies and cumulus-topped conditions. In clear sky days, the insects layer "jumps" higher than the growing mixed-layer early in the morning, but remain very close to the mixed-layer top defined by the RWP after 13:00 LST. In cumulus-topped conditions, the insect layer top estimate remains slightly below the cloud base height throughout the day. This is consistent with previous studies of insects at the SGP ACRF (Luke et al., 2008).

ii. Vertical Velocity Variance Profiles

Profiles of vertical velocity variance and skewness have been frequently explored to characterize convective conditions and the source of turbulent kinetic energy (TKE) in the boundary layer (e.g., LeMone, 1990; Moyer and Young; 1991 Hogan et al., 2008). These profiles are often scaled with the boundary layer height (z_i) in order to provide non-dimensional vertical

coordinates for the daytime turbulent statistics in the planetary boundary layer (e.g., Lenschow et al, 1980; Young 1988). As in the previous sections, during clear sky conditions the mixed-layer height deduced by the RWP is used to scale the vertical coordinate. During cloudy conditions, the hourly averaged cloud base height is used. For each hour of observations and at each MMCR range gate from the surface to the top of the insect layer, the variance of the vertical air motion ($\overline{w'^2}$) is calculated based on time-series of MMCR mean Doppler velocity measurements. The variance values are normalized by the convective velocity scale (w_*) as in (1).

Fig. 3 shows the daytime evolution of the normalized vertical velocity variance profile for cloudy and clear sky conditions. The profiles are smooth due to the large number of hours included in the analysis. In both clear and cloudy conditions, a gradual increase in the magnitude of the normalized variance is observed with time. The maximum values are observed at 15:00 LST. After the maximum at 15:00 LST, hourly profiles from 16:00-18:00 LST exhibit a decrease of the normalized variance magnitude. The 16:00-18:00 LST profiles are very similar to the profiles from 12:00-14:00 LST and thus are omitted for clarity. In the vertical profile, the maximum variance is observed between 0.2 - 0.4 in normalized height. This observation is consistent with a well-mixed boundary layer, where forcing is provided from the bottom (surface) in the form of surface buoyancy flux that is driven mainly by the surface sensible heat flux in our case. The quantity is maximized at the surface and found to decreases linearly towards top of the mixed layer (e.g., Garratt 1992).

The normalized variance profiles for clear and cloud periods have similarities with respect their magnitude and daytime evolution. A noticeable difference is observed during the clear period, above the observed maximum in normalized variance, where the magnitude of the observed normalized variance is shown to decreases linearly with height. This is consistent with

a drop in turbulent kinetic energy as we move away from the source (surface). In contrast, the profiles for cloudy boundary layers exhibit a more complicated structure above 0.4 normalized height. Here, there is an initial decrease in variance as we move away from the surface, but a reversal and the development of a secondary maximum near 0.8 normalized height, the highest level of insect returns. This suggests that in cumulus-topped boundary layers clouds play role in the turbulent budget of the boundary layer. This claim is further investigated by exploring the partitioning of the cloudy profiles of normalized variance at 15:00 LST with respect the observed cloud amount (Fig. 4). The results show that increase in cloudiness is associated with higher normalized variance near the top of the boundary layer and a double peak structure that indicates a secondary source of turbulence near the top of the boundary layer.

Fig. 5 contains composite profiles of normalized vertical velocity variance for clear-sky and cumulus-topped conditions. Two analytical profiles that predict the profile of normalized vertical velocity variance with only input the height of the convective boundary layer are shown for comparison. The symmetric profile proposed by Sorbjan (1989) and the asymmetric profile proposed by Lenschow et al. (1980). The range of observed normalized vertical velocity variance values are within the predicted theoretical values by the two analytical profiles. Our observations agree also with the location of the peak with the asymmetric profile by Lenschow et al. (1980).

iii. Vertical Velocity Skewness Profiles

In addition to the normalized variance, the hourly profiles of vertical velocity skewness are estimated using the MMCR Doppler velocities for both clear and cloudy periods. The skewness is defined as

$$s = \overline{w'^3} \Big/ \overline{w'^2}^{3/2}, \quad (2)$$

where w' is the turbulent component of vertical velocity. The sign of the skewness is driven by asymmetries in the distribution of vertical velocities in a particular height. Positive skewness indicates the presence of few narrow strong updrafts and negative skewness indicates the presence of a few narrow downdrafts in our observations. In a surface driven well-mixed boundary layer, one expects the skewness to be positive and increasing with height. In a top driven boundary layer, one expects the skewness to be negative at the top.

Fig. 6 shows the profiles of vertical velocity skewness for cumulus-topped and clear boundary layer conditions as a function of the normalized boundary layer depth. During clear-sky conditions, skewness values are positive with magnitudes that range from 0.1 to 0.4. Near the surface, the highest values are observed in the late morning hours (11:00 – 12:00 LST) and the lowest values observed during the early afternoon (14:00-15:00 LST) when we have the maximum turbulent activity. In the normalized height range between 0.3 – 0.6, there is no noticeable difference in the skewness value for different times. Thus, during the 14:00 and 15:00 LST hours, we observe the highest vertical gradients in vertical velocity skewness. Above 0.6 normalized heights, the skewness magnitude decreases, but remains positive through out the boundary layer depth.

Within cumulus-topped boundary layer conditions, both positive and negative skewness values are observed. In the low- and mid-level boundary layer heights, positive skewness is observed. The maximum positive skewness (0.3) is observed in the middle of the boundary layer, however, the observed magnitude (0.3) is among the lowest values of skewness calculated during the cloud-free periods in the mid-level. Furthermore, above 0.6 normalized boundary layer heights, a sharp decrease in the skewness and a change in the sign of the skewness near the

insect layer top (0.7-0.8 normalized boundary layer height) is observed. This is an indication of the influence of the cumulus field in the turbulence budget of the boundary layer. Composite profiles of vertical velocity skewness for cumulus-topped boundary layer conditions stratified according to cloud fractions are found in Fig. 7. The analysis reveals that increase in cloud amount (fraction) decreases the skewness magnitude. Negative values are observed in the upper half of the boundary layer, but only for the events featuring higher cloud fractions.

iv. Plume Dimension and Updraft Mass Flux Profiles

During clear sky conditions, coherent updraft and downdraft plume structures exhibit very similar daytime evolution of their normalized half widths (Table 5). The maximum updraft halfwidth (0.53) is observed during morning hours (08:00-9:00 LST) and the minimum (0.3) during late afternoon (16:00-17:00 LST). During cumulus-topped conditions, a similar pattern is observed with the maximum (0.47) observed in the morning hours (08:00-9:00 LST) and the minimum (0.28) in the late afternoon (14:00-15:00 LST). The statistics of the width of the updraft structures change little when the velocity threshold for the plumes from 0 ms^{-1} to 0.6 ms^{-1} is increased, indicating the strength of the updraft plumes. Similar results are found for downdraft halfwidths (Table 5).

As with the vertical velocity variance and skewness profiles, an updraft mass flux is calculated for both clear and cumulus-topped boundary layer conditions. The updraft mass flux is calculated using both a 'direct' and conditional sampling method. Here, the ‘direct’ method estimates total updraft mass flux using all the available upward MMCR velocities at each MMCR range gate. Thus, in this ‘direct’ approach, all upward MMCR Doppler velocity points

contribute to the updraft mass flux calculation. Moreover, this calculation does not discriminate as to whether these measurements are associated with an updraft plume.

The alternate 'conditional sampling' method estimates the updraft mass flux from observations that have an upward MMCR velocity and are also part of a coherent updraft plume according to the criteria outlined in Section 3.2. In the conditional sampling method, not all MMCR upward velocity observations contribute to the estimated mass flux (Kollias and Albrecht, 2000). It is noted that if the velocity field is completely incoherent (spectrum is white), the conditional sampling method updraft mass flux will approach zero. Similarly, if the velocity field is completely coherent (e.g. a sine wave) the updraft mass flux estimated by the conditional sampling method will equal the updraft mass flux estimated with the direct method. Therefore, the ratio of the updraft mass flux from the conditional sampling and direct sampling methods indicates the amount of turbulent transport in the boundary layer from coherent plume (e.g. large eddies).

The daytime evolution of the updraft mass flux in the mixed-layer during clear-sky conditions is shown in Fig. 8. The updraft mass flux profiles cover the period from 11:00 to 15:00 LST and their calculation is based on both the "direct" and "conditional" sampling method. The profiles of updraft mass flux increase to a maximum at z/zi = 0.3 and then decrease almost linearly with normalized height to reach their lowest value at the maximum height of our observations (z/zi = 0.9). The daytime variability is more pronounced in the lower part of the mixed-layer and the largest values are observed at 13:00 LST. The comparison of the updraft mass flux profiles by the "direct" and "conditional" sampling method indicates that coherent structures with minimum dimensions 225 m in the vertical and 150-300 m in the horizontal are responsible for most of the turbulent transport in the mixed-layer during clear sky conditions.

The daytime evolution of the updraft mass flux in the subcloud layer during cumulus-topped conditions is shown in Fig. 9. The profiles of updraft mass flux exhibit structure similar to the ones observed for clear-skies. The maximum updraft mass flux is observed at z/zi = 0.3; a decrease is observed with height above the location of the maximum and the highest updraft mass flux values are observed at 13:00 LST. Another similarity between clear-sky and cumulus-topped periods is the observation that coherent structures are responsible for the bulk of the turbulent transport. However, on average, the updraft mass flux magnitudes calculated during cumulus-topped periods are smaller than these observed during clear-sky periods. For instance, at 13:00 LST, the maximum is 0.58 $Kgm^{-2}s^{-1}$ for clear-sky and 0.47 $Kgm^{-2}s^{-1}$ for cumulus-topped conditions. Furthermore, near the top of the subcloud layer, a reversal in the decreasing trend of the updraft mass flux calculated by the "direct" method is observed. This is manifested by a small increase of the updraft mass flux at the top of the subcloud layer (z/zi~0.9). This finding hints at the potential impact of the cloud layer in the turbulent transport of the subcloud layer. Another interesting observation is that the small reversal in updraft mass flux near the top of the subcloud layer is not detected using the "conditional" method. This observation suggests that the horizontal and/or vertical scale of the vertical velocity structures responsible for the observed changes in the vertical structure of the updraft mass flux near the subcloud layer top are smaller than the minimum dimensions set in the "conditional" sampling method.

5. SUMMARY

Insect radar returns at the SGP ACRF have been long considered as a nuisance in our effort to use ground-based vertically pointing radars to detect and study boundary layer clouds. In this study, a different approach is adopted and the insect radar returns from vertically pointing Doppler cloud radar are used to monitor the properties of boundary-layer turbulence. The study makes use of a multi-year summer dataset from millimeter-wavelength cloud radar, a 915-MHz wind profiler and flux measuring sensors at the surface.

The large dataset (2,894 hours) is classified into clear-sky and cumulus-topped conditions. During clear-sky conditions, the 915-MHz wind profiler signal to noise ratio is used to develop an automated algorithm for the detection of the mixed-layer top. During cumulus-topped conditions, the cloud base detections from the lidar are used to estimate the top of the subcloud layer. The daytime evolution of the boundary layer is studied using the profiles of vertical velocity variance and skewness. The normalized vertical velocity variance profiles exhibit a smooth daytime evolution with the maximum turbulent activity observed near 15:00 LST. During clear-sky conditions the maximum is observed around z/zi = 0.3 which fits very well the past aircraft observations for surface-driven turbulence. During cumulus-topped conditions, a secondary maximum is observed near the top of the subcloud layer indicating the influence of the cloud layer in the subcloud layer turbulence. The vertical velocity skewness profiles for clear-skies conditions are positive. This is consistent with a surface-drive boundary layer. During cumulus-topped conditions, negative skewness is observed near the top of the subcloud layer indicating the role of the cloud layer and the existence of narrow penetrating downdrafts in the subcloud layer.

Using a conditional sampling method, coherent vertical velocity structures in the boundary layer are detected. Updraft mass flux calculations using direct sampling and the conditional sampling technique exhibit that coherent structures (eddies) are responsible for more than 80% of the total turbulent transport observed by the radar in the boundary layer for both clear skies and cumulus-topped conditions. However, clear-skies periods have on average higher updraft mass flux and cumulus-topped periods have higher updraft mass flux near the top of the subcloud layer due to the influence of clouds.

Overall, the characterization of the boundary layer turbulence using insect radar returns are consistent with previous aircraft observations and suggested analytical profiles. The observations provided a unique daytime evolution of the convective boundary layer and indicate the role of increased cloudiness in the turbulent budget of the subcloud layer. The large data set makes the observations suitable for evaluating boundary-layer parameterizations for a variety of surface and cloud conditions.

6. ACKNOWLEDGEMENTS

Support for this research was funded by the Office of Biological and Environmental Research, Environmental Sciences Division of the U.S. Department of Energy as part of the Atmospheric Radiation Measurement program. The contribution of S. A. Klein to this work is performed under the auspices of the U. S. Department of Energy by Lawrence Livermore National Laboratory under contract DE-AC52-07NA27344.

7. REFERENCES

Achtemeier, G. L., 1991: The Use of Insects as Tracers for "Clear-air" Boundary-Layer Studies by Doppler Radar, *Journal of Atmos. and Ocean. Tech,* 8, 746-765.

Ackerman, T. P., and G. Stokes, 2003: The Atmospheric Radiation Measurement program, *Phys. Today*, 56, 38-45.

Betts, 1976: Modeling subcloud layer structure and interaction with a shallow cumulus layer. *J. Atmos. Sci*. 33, 2363-2382.

Bony, S., R. Colman, V.M. Kattsov, R.P. Allan, C.S. Bretherton, J.L. Dufresne, A. Hall, S. Hallegatte, M.M. Holland, W. Ingram, D.A. Randall, B.J. Soden, G. Tselioudis, and M.J. Webb, 2006: How Well Do We Understand and Evaluate Climate Change Feedback Processes? *J. Climate*, **19**, 3445–3482.

Brown, A. R., Cederwall, R. T., A. Chlond, P. G. Duynkerke, J. C. Golaz, M. Khairoutdinov, D. C. Lewellen, A. P. Lock, M. K. Macvean, C. H. Moeng, R. A. J. Neggers, A. P. Siebesma, and B. Stevens, 2002: Large-eddy simulation of the diurnal cycle of shallow cumulus convection over land. *Quart. J. Roy. Meteor. Soc*., 128, 10875-1093.

Brummer, B., 1978: Mass and energy budgets of a 1 km high atmospheric box over the GATE C-scale triangle during undisturbed and disturbed weather conditions. *J. Atmos. Sci*. 35, 997-1011.

De Roode, S. R. and Bretherton, C. S., 2003: Mass flux budgets of shallow cumulus. *J. Atmos. Sci.*, 60, 137–151.

Echternacht, K. L., and M. Garstang, 1976: Changes in the structure of the tropical subcloud layer from the undisturbed to the disturbed states. *Mon. Wea. Rev.,* 104, 407-417.

Edward, P. Luke, Pavlos Kollias, and Karen, L. Johnson, 2008: A Technique for the Automatic Detection of Insect Clutter in Cloud Radar Returns. *Journal of Atmos. and Ocean. Tech*, 25, 1498-1513.

Eugene, E. Clothiaux, Thomas, P. Ackerman, Gerald, G. Mace, Kenneth, P. Moran, Roger, T. Marchand,* Mark A. Miller, and Brooks, E. Martner, 2000: Objective determination of cloud heights and radar reflectivities using a combination of active remote sensors at the ARM CART Sites. *Journal of Appl Meteor*, 39, 645-665.

French, J.F., G. Vali, and R.D. Kelly, 2000: Observations of microphysics pertaining the development of drizzle in warm, shallow cumulus clouds. *Quart. J. Royal. Meteor. Soc*., 126 (563), 415-443.

Garratt, J. R., 1992: *The atmospheric boundary layer.* Cambridge, 316 pp.

Geerts, B., and Q. Miao, 2005a: The use of millimeter Doppler radar echoes to estimate vertical air velocities in the fair-weather convective boundary layer. *J. Atmos. Oceanic Technol.* 22, 225–246.

Johnson, R. H., 1977: Effects of cumulus convection on the structure and growth of the mixed layer over south Florida. *Mon. Wea. Rev.,*105, 713-724.

Kaimal, J. C., and Coauthors 1976: 'Turbulent Structure in the Convective Boundary Layer'. *J. Atmos. Sci*. 33, 2152-2169.

Kaimal, J. C., and Finnigan, J. J., 1994: Atmospheric boundary layer flows – their structure and measurement. *Oxford University Press*, Newyork.

Kollias, P., R. Lhermitte and B.A. Albrecht, 1999 Vertical air motion and raindrop size distributions in convective systems using a 94 GHz radar. *Geophys. Res. Lett.* 26 (20), 3109-3112.

Kollias, P. and B. Albrecht, 2000. The turbulence structure in a continental stratocumulus cloud from millimeter wavelength radar observations. ***J. Atmos. Sci.* 57**, 2417-2434.

Kollias, P., B.A. Albrecht, R. Lhermitte and A. Savtchenko, 2001a. Radar observations of updrafts, downdrafts, and turbulence in fair weather cumuli. ***J. Atmos. Sci.* 58**, 1750-1766.

Kollias, P., B.A. Albrecht and F.D. Marks, Jr., 2002. Accurate observations of vertical air velocities and rain drops using a cloud radar - Why mie?. ***Bull. Amer. Meteor. Soc,*** **83,** 1471–1483**.**

Kollias, P., E.E. Clothiaux, M.A. Miller, B.A. Albrecht, G.L. Stephens, and T.P. Ackerman, 2007: Millimeter-Wavelength Radars: New Frontier in Atmospheric Cloud and Precipitation Research. Bull. Amer. Meteor. Soc., 88, 1608–1624.

Kusuma, G., Rao, and R, Narasimha, 2006: Heat- flux scaling for weakly forced turbulent convection in the atmosphere. *Journal of Fluid Mechanics.,* 547, 115-135.

Lemone, M. A., and W. T. Pennell, 1976: The relationship of trade wind cumulus distribution to subcloud layer fluxes and structure. *Mon. Wea. Rev*., 104, 524-539.

Lemone, M. A., 1990: Some observations of vertical velocity skewness in the convective planetary boundary layer. *J. Atmos. Sci*., 47, 1163-1169.

Lenderink, G and Co-authors, 2004: The diurnal cycle of shallow cumulus clouds over land: A single –column model intercomparison study. *Quart. J. Roy.Meteor. Soc.,* 130, 3339-3364.

Lenschow, D. H. 1970: 'Airplane Measurements of Planetary Boundary Layer Structure'. J. *Appl. Meteorol*, 9, 874-884.

Lenschow, D. H., J. C. Wyngaard and W.T. Pennell, 1980: Mean-field and second-moment budgets in a baroclinic, convective boundary layer. *J. Atmos. Sci.,* 37, 1313–1326.

Moran, K. P., B. E. Martner, M. J. Post, R. A. Kropfli, D. C. Welsh, and K. B. Widener, 1998: An unattended cloud-profiling radar for use in climate research. *Bull. Amer. Meteor. Soc.,* 79, 443–455.

Moyer KA, Young GS. 1991. Observations of vertical velocity skewness within the marine stratocumulus-topped boundary layer. *J. Atmos. Sci.* **48**: 403–410.

R. A. J. Neggers, P. G., Duynkerke and S. M. A. Rodts, 2003: Shallow cumulus convection: A validation of large-eddy simulation against aircraft and Landsat observations. *Q. J. R. Meteorol. Soc,* 129, 2671–2696.

Nicholls, S. and M.A. LeMone, 1980: The Fair Weather Boundary Layer in GATE: The Relationship of Subcloud Fluxes and Structure to the Distribution and Enhancement of Cumulus Clouds. *J. Atmos. Sci*. 37, 2051-2067.

Norris, J. R. 1998: Low cloud type over the ocean from surface observations. part II: Geographical and seasonal variations. J. Clim., 11, 383–403.

Qun Miao, Bart Geerts and Lemone, 2006: Vertical Velocity and Buoyancy Characteristics of Coherent Echo Plumes in the Convective Boundary Layer, Detected by a Profiling Airborne Radar. *Journal of Applied Meteorology and Climatology., 45, 838-855.*

Randall D. A., Q. Shao, and C.H. Moeng, 1992: A second-order bulk boundary-layer model. *J. Atmos. Sci.*, 49, 1903–1923.

Riley, J. R., 1992: A millimetric radar to study the flight of small insects. Electronics & Communication Engineering Journal, 4, 43-48.

Rio, C., and F. Hourdin, 2008: A Thermal Plume Model for the Convective Boundary Layer: Representation of Cumulus Clouds. *J. Atmos. Sci.*, **65**, 407–425

Robin, J. Hogan, Alan, L. M. Grant, Anthony, J. Illingworth, Guy, N. Pearson and Ewan, J. O'Connor, 2008: Vertical velocity variance and skewness in clear and cloud-topped boundary layers as revealed by Doppler Lidar. *Q. J. R. Meteorol. Soc,* 135, 635–643.

Russell, R. W., and J. W. Wilson, 1997: Radar-observed "fine lines" in the optically clear boundary layer: Reflectivity contributions from aerial plankton and its predators. *Bound.-Layer Meteor.,* 82, 235–262.

Schumann, U. and Moeng, C.-H. 1991: Plume budgets in clear and cloudy convective boundary layers. *J. Atmos. Sci.*, 48, 1758–1770.

Siebesma, and Coauthors, 2003: A large eddy simulation intercomparison study of shallow cumulus convection. *J. Atmos. Sci.*, 60, 1201–1219.

Siebesma, A. P. and Cuijpers, J. W. M, 1995: Evaluation of parametric assumptions for shallow cumulus convection. *J. Atmos. Sci.*, 52, 650–666.

Siebesma, A.P., P.M.M. Soares, and J. Teixeira, 2007: A Combined Eddy-Diffusivity Mass-Flux Approach for the Convective Boundary Layer. *J. Atmos. Sci.*, **64**, 1230–1248.

Sorbjan, Z., 1989: *Structure of the atmospheric boundary layer.* Prentice Hall, New Jersey, 317 pp.

Stevens, B., A. S. Ackerman, B. A. Albrecht, A. R. Brown, A. Chlond, J. Cuxart, P. G. Duynkerke, D. C. Lewellen, M. K. Macvean, R. A. J. Neggers, E. Sa'nchez, A. P. Siebesma and D. E. Stevens, 2001: Simulations of trade wind cumuli under a strong inversion. J. Atmos. Sci., 58, 1870-1891.

Stokes, G. M., and S. E. Schwartz, 1994: The Atmospheric Radiation Measurement (ARM) Program: Programmatic Background and Design of the Cloud and Radiation Test Bed. *Bull Amer. Meteor. Soc.*, **75,** 1201-1222.

Teixeira, J., B. Stevens, C.S. Bretherton, R. Cederwall, J.D. Doyle, J.C. Golaz, A.A.M. Holtslag, S.A. Klein, J.K. Lundquist, D.A. Randall, A.P. Siebesma, and P.M.M. Soares, 2008:

Parameterization of the Atmospheric Boundary Layer: A View from Just Above the Inversion. *Bull. Amer. Meteor. Soc*., 89, 453–458.

Thompsom, N., K. L., Webber and B.P. Norris, 1980: Eddy fluxes and spectra in the GATE subcloud layer. *Quart. J. Roy.Meteor. Soc.,* 106, 277-292.

Tiedtke, M., 1989: A Comprehensive Mass flux scheme for cumulus parameterization in large scale models. *Month. Wea. Rev*. 117, 1799-1801.

Wang, S. and Stevens, B. 2000: Top-hat representation of turbulence statistics in cloud-topped boundary layers: A large-eddy simulation study. *J. Atmos.Sci.*, 57, 423–441.

Warner, J., 1977: Time variation of updraft and water content in small cumulus clouds. *J. Atmos. Sci.,* 34, 1306–1312.

J. M. Wilczak, E. E. Gossard, W. D. Neff and W. L. Eberhard, 1996: Ground-based remote sensing of the Atmospheric Boundary Layer: 25 years of progress. *Boundary-Layer Meteorol*, 78, 321-349.

Young, G. S., 1988: Turbulence structure of the convective boundary layer - 1. Variability of normalized turbulence statistics. *J. Atmos.* Sci. 45, 719–726.

9. FIGURE CAPTIONS

Figure 1. Example of time-height mapping of (a) MMCR reflectivity factor during a cumulus-topped event on July 22, 2006; Red dots indicate the cloud base as measured from a ceilometer. (b) MMCR Doppler velocity for the 12:00-13:00 UTC time period. (c) Diurnal variation of Radar Wind Profiler (RWP) signal to noise ratio (SNR) during a clear-sky day on June 20, 2006. Black diamonds indicate the algorithm retrieved mixed layer heights based on SNR gradient and red cross indicates are the mixed layer heights estimated using the virtual potential temperature profile from rawinsondes launched at 11:00 and 17:00 local time.

Figure 2. Daytime evolution of the insect layer top for cumulus-topped (top) and clear-sky conditions (bottom). In addition to the insect layer top, the daytime evolution of the cloud base height from the ceilometer (top) and mixed-layer depth from the RWP (bottom) are shown.

Figure 3. Daytime evolution of the composite profiles of (a) normalized vertical velocity variance during cumulus-topped conditions; the zi for shallow cumulus conditions is estimated from the cloud base heights detected by the ceilometer; (b) normalized vertical velocity variance during the clear-sky condition; the zi for clear-sky conditions is estimated from the mixed layer depth retrieval using the Radar Wind Profiler signal-to-noise ratio.

Figure 4. Averaged profiles of the normalized vertical velocity variance during clear sky and cumulus-topped conditions for three different cloud fraction (CF) regimes. Low CF: 0<CF<=0.2, Moderate CF: 0.2<CF<=0.6, High CF: 0.6<CF<1.0. Only the profiles collected in the three hour period 14:00 – 17:00 LST are used in the averaging.

Figure 5. Comparison of the composite profiles of normalized vertical velocity variance for cumulus-topped (circles) and clear-sky (stars) conditions with reference analytical profile calculations fitted to the observations. The symmetric profile of Sorbjan (1989) is the fit to the observations in cloudless boundary layers (upward pointing triangles). The asymmetric profile (downward pointing triangles) is the fit to the observations by Lenschow et al. (1980). Only measurements collected between 12:00 to 16:00 LST are shown in the figure.

Figure 6. Daytime evolution of the composite profiles of (a) vertical velocity skewness during cumulus-topped conditions; the zi for shallow cumulus conditions is estimated from the cloud base heights detected by the ceilometer; (b) vertical velocity variance skewness during the clear-sky condition; the zi for clear-sky conditions is estimated from the mixed layer depth retrieval using the Radar Wind Profiler signal-to-noise ratio.

Figure 7. Averaged profiles of the vertical velocity skewness during clear sky and cumulus-topped conditions for three different cloud fraction (CF) regimes. Low CF: 0<CF<=0.2,

Moderate CF: 0.2<CF<=0.6, High CF: 0.6<CF<1.0. Only the profiles collected in the three hour period 14:00 – 17:00 LST were used in the averaging.

Figure 8. Daytime evolution of the composite profiles of the mass flux as calculated during clear-sky conditions. (a) Total mass flux calculated from a 'direct' method capitalizing on all upward values of the vertical velocity. (b) Mass flux attributed to coherent structures only based on the conditional sampling method. For normalization of these plots, zi is the mixed-layer height.

Figure 9. Daytime evolution of the composite profiles of the mass flux as calculated during shallow cumulus conditions. (a) Total mass flux calculated from a 'direct' method capitalizing on all upward values of the vertical velocity. (b) Mass flux attributed to coherent structures only based on the conditional sampling method. For normalization of these plots, zi is the cloud base height.

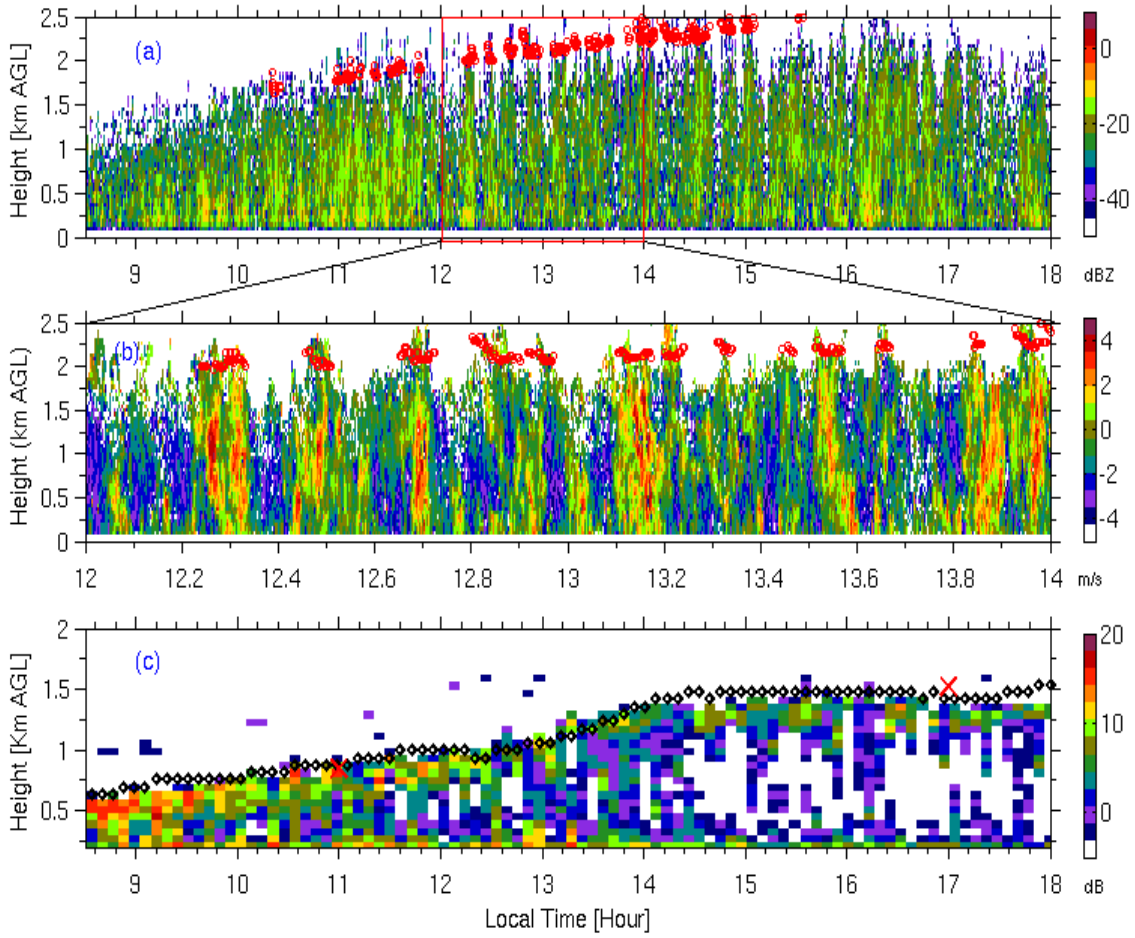

Figure 1. Example of time-height mapping of (a) MMCR reflectivity factor during a cumulus-topped event on July 22, 2006; Red dots indicate the cloud base as measured from a ceilometer. (b) MMCR Doppler velocity for the 12:00-13:00 UTC time period. (c) Diurnal variation of Radar Wind Profiler (RWP) signal to noise ratio (SNR) during a clear-sky day on June 20, 2006. Black diamonds indicate the algorithm retrieved mixed layer heights based on SNR gradient and red cross indicates are the mixed layer heights estimated using the virtual potential temperature profile from rawinsondes launched at 11:00 and 17:00 local time.

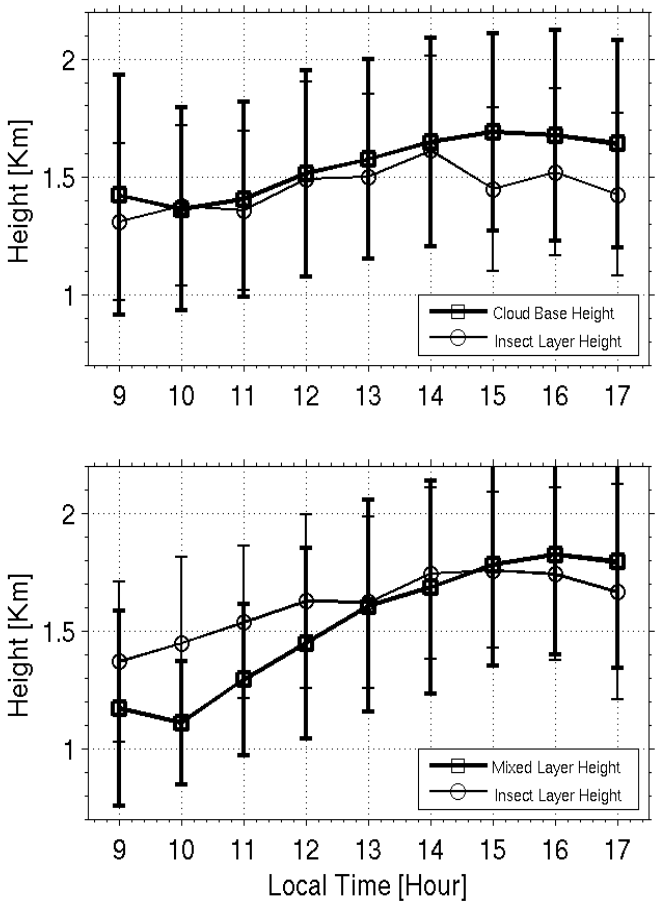

Figure 2. Daytime evolution of the insect layer top for cumulus-topped (top) and clear-sky conditions (bottom). In addition to the insect layer top, the daytime evolution of the cloud base height from the ceilometer (top) and mixed-layer depth from the RWP (bottom) are shown.

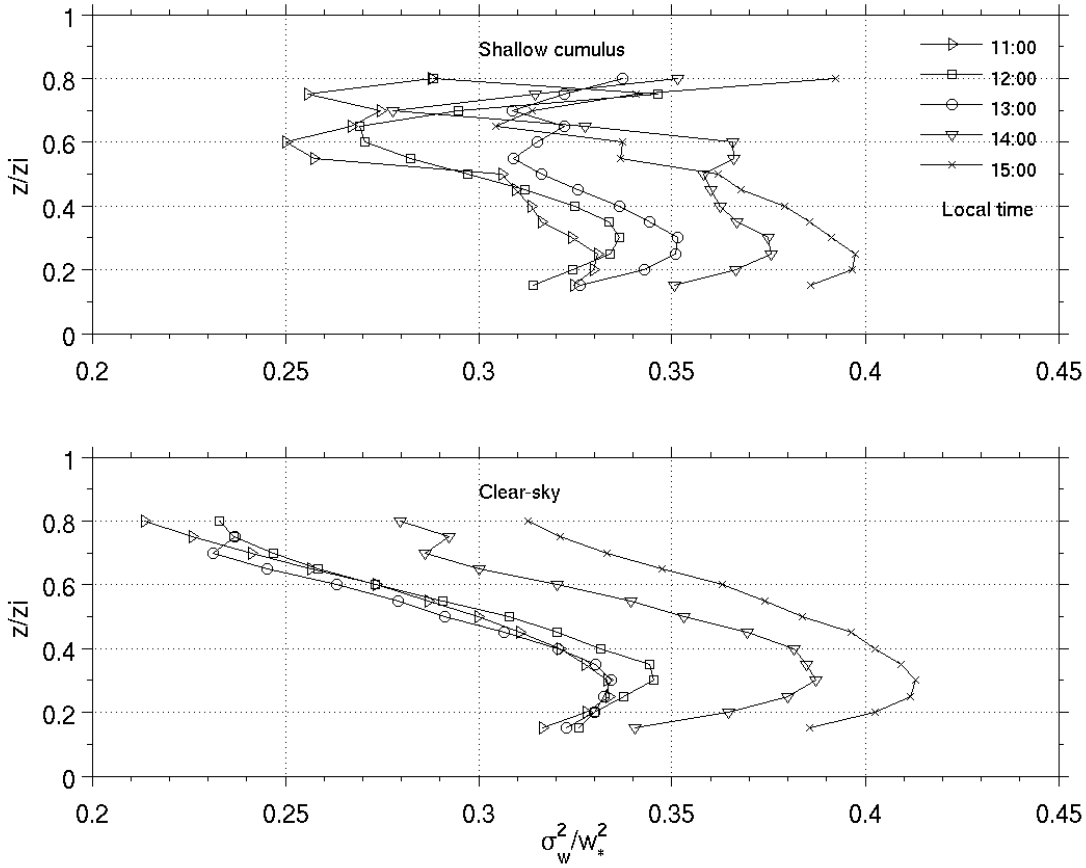

Figure 3. Daytime evolution of the composite profiles of (a) normalized vertical velocity variance during cumulus-topped conditions; the zi for shallow cumulus conditions is estimated from the cloud base heights detected by the ceilometer; (b) normalized vertical velocity variance during the clear-sky condition; the zi for clear-sky conditions is estimated from the mixed layer depth retrieval using the Radar Wind Profiler signal-to-noise ratio.

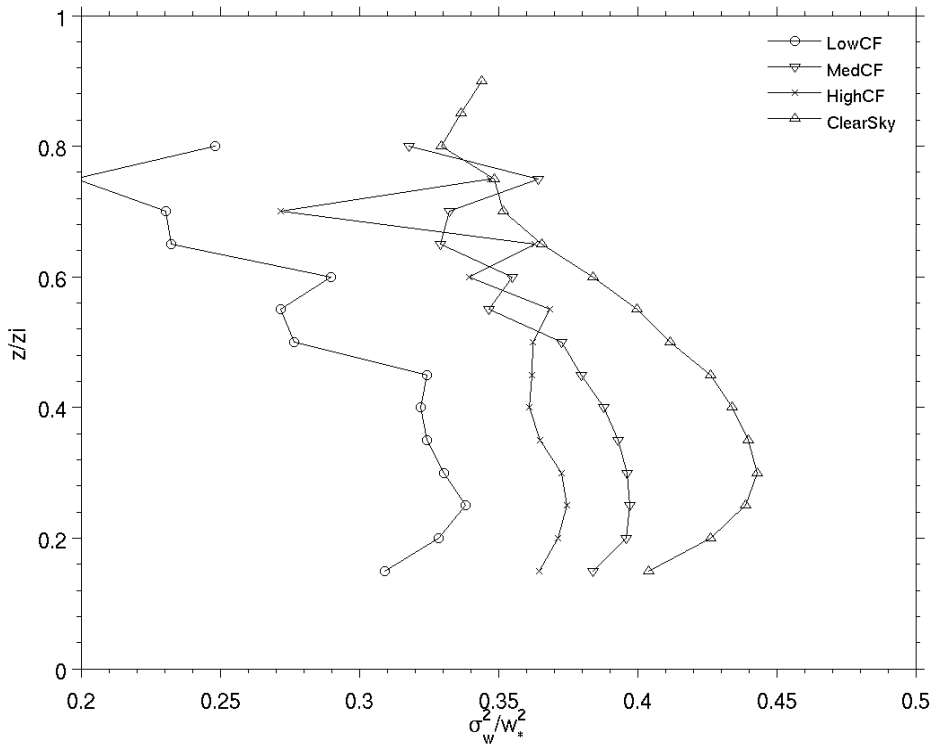

Figure 4. Averaged profiles of the normalized vertical velocity variance during clear sky and cumulus-topped conditions for three different cloud fraction (CF) regimes. Low CF: 0<CF<=0.2, Moderate CF: 0.2<CF<=0.6, High CF: 0.6<CF<1.0. Only the profiles collected in the three hour period 14:00 – 17:00 LST are used in the averaging.

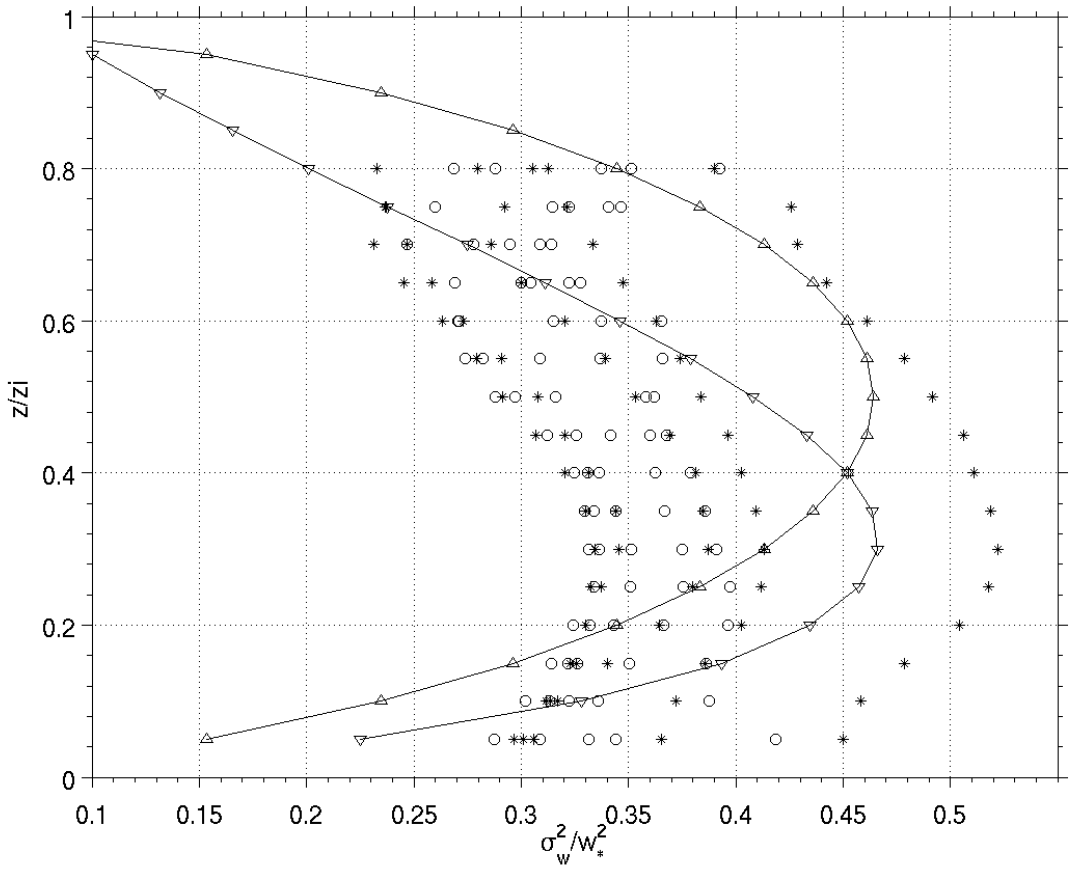

Figure 5. Comparison of the composite profiles of normalized vertical velocity variance for cumulus-topped (circles) and clear-sky (stars) conditions with reference analytical profile calculations fitted to the observations. The symmetric profile of Sorbjan (1989) is the fit to the observations in cloudless boundary layers (upward pointing triangles). The asymmetric profile (downward pointing triangles) is the fit to the observations by Lenschow et al. (1980). Only measurements collected between 12:00 to 16:00 LST are shown in the figure.

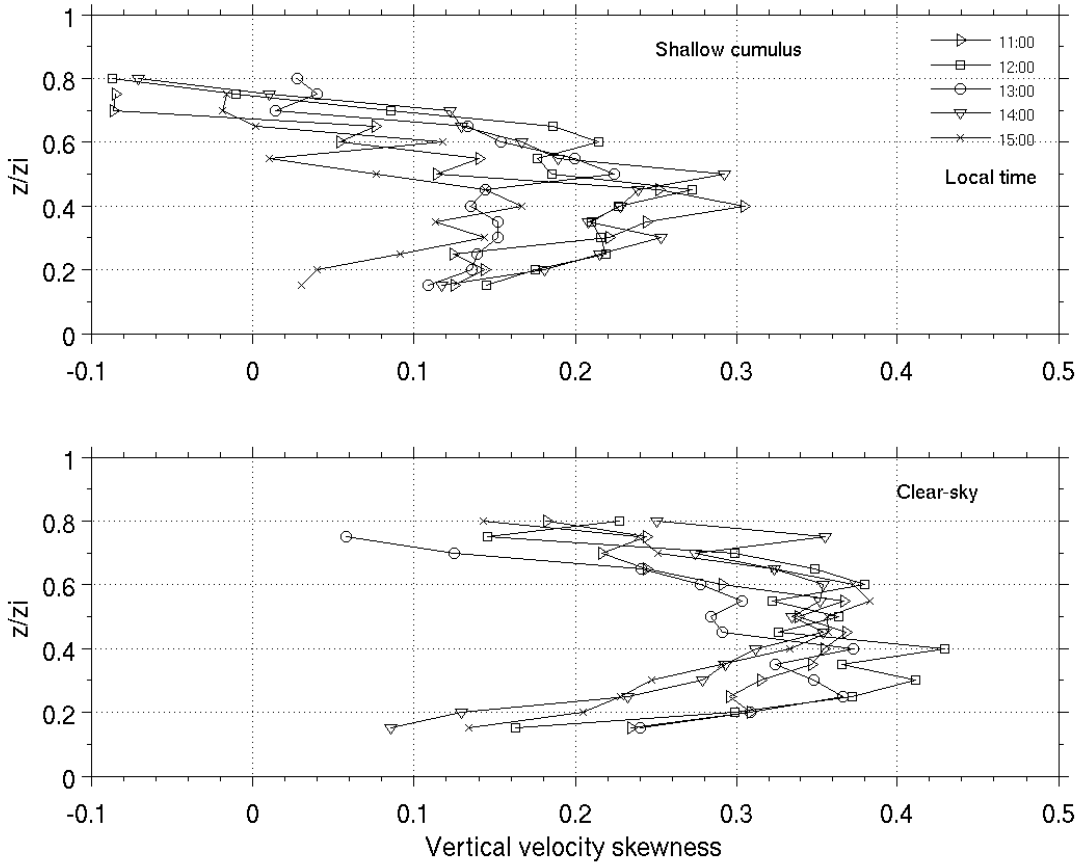

Figure 6. Daytime evolution of the composite profiles of (a) vertical velocity skewness during cumulus-topped conditions; the zi for shallow cumulus conditions is estimated from the cloud base heights detected by the ceilometer; (b) vertical velocity variance skewness during the clear-sky condition; the zi for clear-sky conditions is estimated from the mixed layer depth retrieval using the Radar Wind Profiler signal-to-noise ratio.

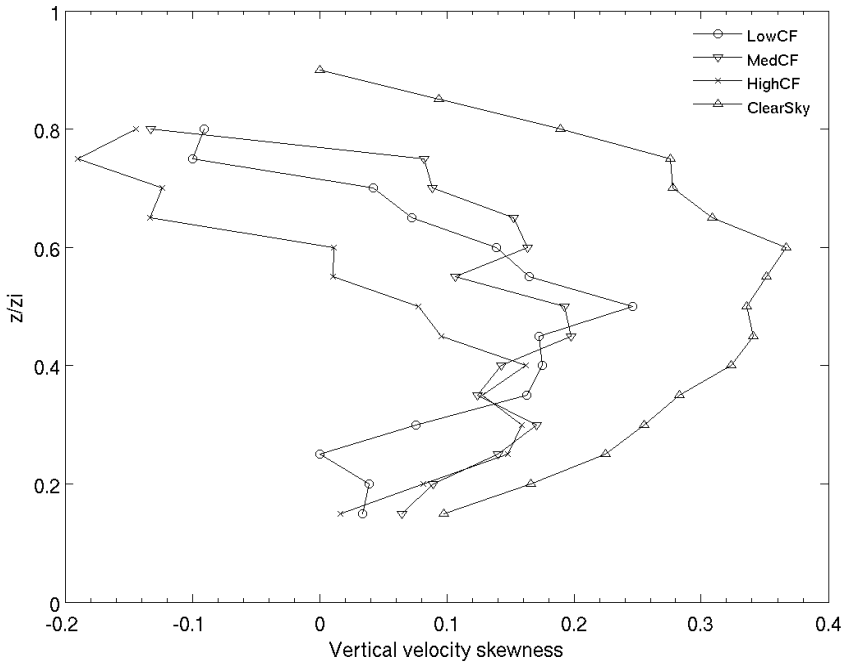

Figure 7. Averaged profiles of the vertical velocity skewness during clear sky and cumulus-topped conditions for three different cloud fraction (CF) regimes. Low CF: 0<CF<=0.2, Moderate CF: 0.2<CF<=0.6, High CF: 0.6<CF<1.0. Only the profiles collected in the three hour period 14:00 – 17:00 LST were used in the averaging.

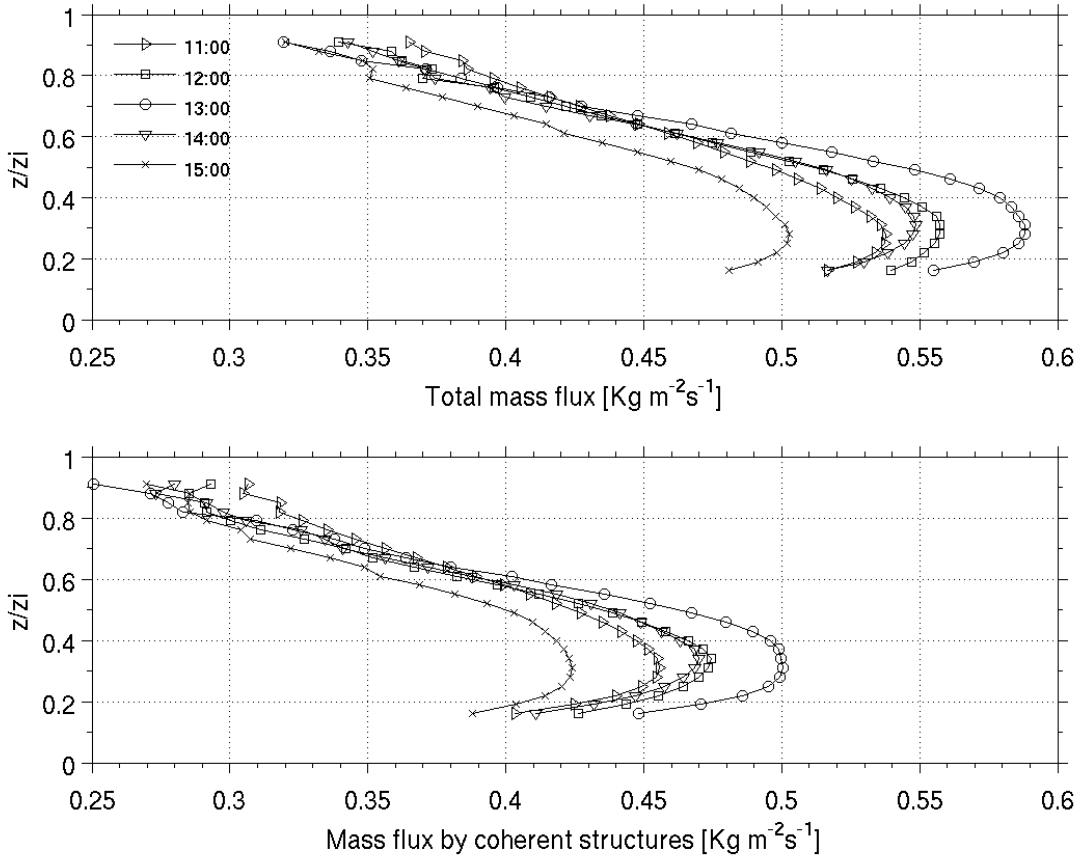

Figure 8. Daytime evolution of the composite profiles of the mass flux as calculated during clear-sky conditions. (a) Total mass flux calculated from a 'direct' method capitalizing on all upward values of the vertical velocity. (b) Mass flux attributed to coherent structures only based on the conditional sampling method. For normalization of these plots, zi is the mixed-layer height.

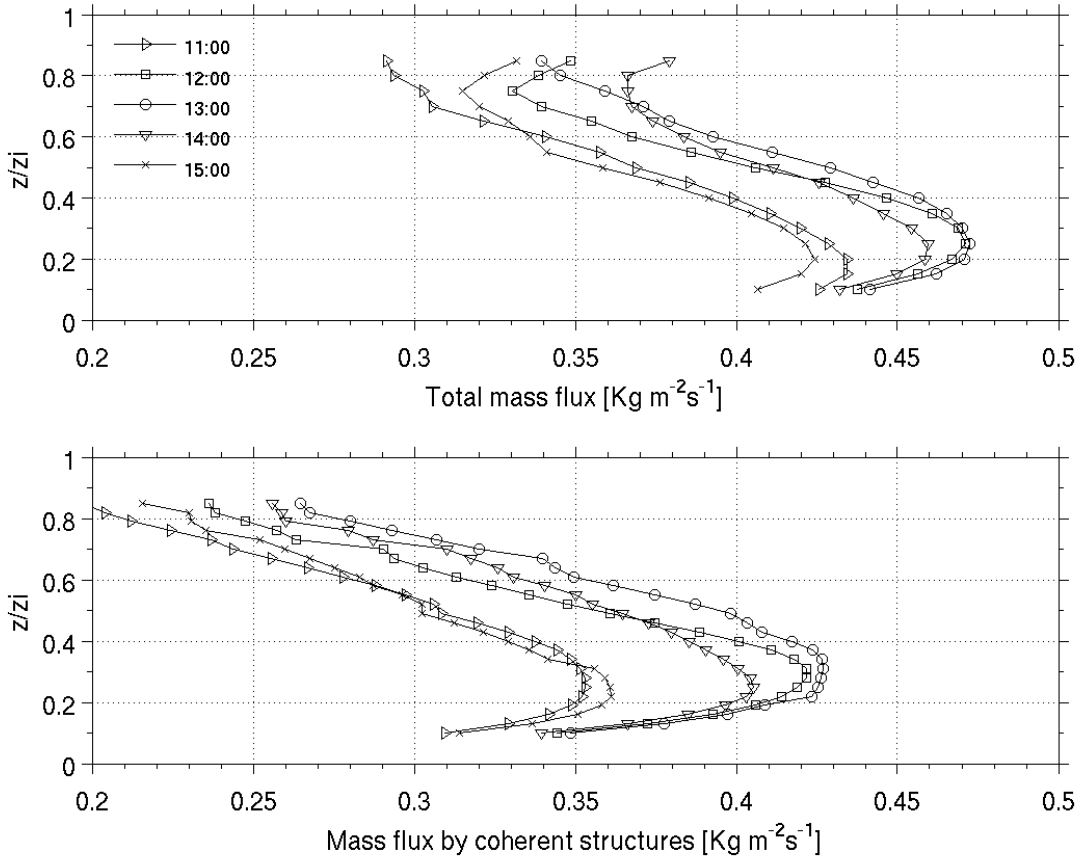

Figure 9. Daytime evolution of the composite profiles of the mass flux as calculated during shallow cumulus conditions. (a) Total mass flux calculated from a 'direct' method capitalizing on all upward values of the vertical velocity. (b) Mass flux attributed to coherent structures only based on the conditional sampling method. For normalization of these plots, zi is the cloud base height.

8. TABLE CAPTIONS

Table 1. Tabulated hourly values (mean and standard deviation) of boundary layer and surface properties during clear-sky conditions at the ARM SGP.

Table 2. Tabulated hourly values (mean and standard deviation) of boundary layer and surface properties during low cloud fraction (below 20%) cumulus conditions at the ARM SGP.

Table 3. Tabulated hourly values (mean and standard deviation) of boundary layer and surface properties during moderate cloud fraction (20-60%) cumulus conditions at the ARM SGP.

Table 4. Tabulated hourly values (mean and standard deviation) of boundary layer and surface properties during high cloud fraction (above 60%) cumulus conditions at the ARM SGP.

Table. 5. Classification of updraft and downdraft half-widths during shallow cumulus and clear-sky events based on time of the day.

Table 1. Tabulated hourly values (mean and standard deviation) of boundary layer and surface properties during clear-sky conditions at the ARM SGP.

Local time (Hr)	**8**	**9**	**10**	**11**	**12**	**13**	**14**	**15**	**16**	**17**
Clear-sky hours (total)	187	188	195	174	157	141	135	144	149	133
Mixed-layer height, mean (m)	648	785	947	1167	1355	1501	1543	1598	1654	1631
Mixed-layer height, std (m)	231	315	286	375	462	524	552	581	575	584
Conv. Velocity, mean (ms^{-1})	1.59	1.70	1.81	1.96	2.03	2.02	1.89	1.81	1.80	1.65
Conv. Velocity, std (ms^{-1})	0.56	0.46	0.41	0.42	0.47	0.49	0.47	0.42	0.46	0.54
Sfc Buoyancy Flux, mean (Wm^{-2})	118	182	231	267	275	271	239	193	131	80
Sfc Buoyancy Flux, std (Wm^{-2})	47	67	77	81	85	80	83	80	63	42

Table 2. Tabulated hourly values (mean and standard deviation) of boundary layer and surface properties during low cloud fraction (below 20%) cumulus conditions at the ARM SGP.

Local time (Hr)	**8**	**9**	**10**	**11**	**12**	**13**	**14**	**15**	**16**	**17**
Cumulus-topped hours (total)	25	27	38	40	41	57	64	52	49	19
Cloud coverage, mean (fraction)	0.052	0.068	0.075	0.076	0.098	0.084	0.093	0.10	0.097	.076
Cloud coverage, std (fraction)	0.044	0.053	0.059	0.05	0.061	0.054	0.063	0.054	0.063	0.058
Cloud Base, mean (m)	1100	1080	1108	1259	1563	1710	1664	1730	1712	1627
Cloud Base, std (m)	675	620	489	484	577	527	545	482	507	524
Sfc Buoyancy Flux, mean (Wm^{-2})	70	121	162	233	195	225	210	164	107	68
Sfc Buoyancy Flux, std (Wm^{-2})	50	64	87	117	106	107	103	88	64	46
Conv. Velocity, mean (ms^{-1})	1.12	1.44	1.61	1.89	1.91	2.09	2.02	1.88	1.60	1.34
Conv. Velocity, std (ms^{-1})	0.35	0.37	0.47	0.59	0.47	0.55	0.52	0.44	0.43	0.32

Table 3. Tabulated hourly values (mean and standard deviation) of boundary layer and surface properties during moderate cloud fraction (20-60%) cumulus conditions at the ARM SGP.

Local time (Hr)	**8**	**9**	**10**	**11**	**12**	**13**	**14**	**15**	**16**	**17**
Cumulus-topped hours (total)	40	33	47	59	54	67	68	68	48	32
Cloud coverage, mean (fraction)	0.374	0.384	0.390	0.388	0.376	0.401	0.375	0.357	0.373	0.387
Cloud coverage, std (fraction)	0.118	0.130	0.105	0.109	0.111	0.119	0.119	0.118	0.110	0.128
Cloud Base, mean (m)	1272	1238	1225	1360	1524	1447	1684	1621	1623	1606
Cloud Base, std (m)	701	604	569	513	458	425	414	488	439	510
Sfc Buoyancy Flux, mean (Wm^{-2})	68	121	153	183	217	213	190	155	108	60
Sfc Buoyancy Flux, std (Wm^{-2})	44	66	96	91	96	88	84	77	67	37
Conv. Velocity, mean (ms^{-1})	1.22	1.50	1.59	1.81	2.01	1.97	1.98	1.81	1.60	1.31
Conv. Velocity, std (ms^{-1})	0.28	0.41	0.40	0.44	0.41	0.36	0.37	0.41	0.40	0.34

Table 4. Tabulated hourly values (mean and standard deviation) of boundary layer and surface properties during high cloud fraction (above 60%) cumulus conditions at the ARM SGP.

Local time (Hr)	**8**	**9**	**10**	**11**	**12**	**13**	**14**	**15**	**16**	**17**
Cumulus-topped hours (total)	26	40	42	45	56	47	45	28	18	16
Cloud coverage, mean (fraction)	0.834	0.805	0.845	0.867	0.836	0.837	0.850	0.881	0.793	0.876
Cloud coverage, std (fraction)	0.140	0.146	0.132	0.122	0.141	0.129	0.130	0.128	0.149	0.121
Cloud Base, mean (m)	1398	1202	1133	1154	1218	1303	1319	1401	1348	1354
Cloud Base, std (m)	582	492	398	394	385	403	432	415	551	438
Sfc Buoyancy Flux, mean (Wm^{-2})	44	84	121	140	154	141	119	93	75	39
Sfc Buoyancy Flux, std (Wm^{-2})	28	49	72	62	68	73	64	64	49	33
Conv. Velocity, mean (ms^{-1})	1.08	1.33	1.45	1.56	1.65	1.60	1.57	1.40	1.26	1.01
Conv. Velocity, std (ms^{-1})	0.33	0.34	0.36	0.31	0.36	0.38	0.37	0.39	0.44	0.31

Table. 5. Classification of updraft and downdraft half-widths during shallow cumulus and clear-sky events based on time of the day.

Local time (Hours)	9	10	11	12	13	14	15	16
Shallow Cumulus Condition								
Updraft Half-width	0.468	0.429	0.377	0.327	0.334	0.327	0.281	0.302
Downdraft Half-width	0.439	0.370	0.383	0.335	0.342	0.318	0.295	0.318
Clear-Sky Condition								
Updraft Half-width	0.530	0.446	0.370	0.324	0.338	0.334	0.333	0.317
Downdraft Half-width	0.576	0.445	0.375	0.331	0.349	0.326	0.337	0.304